

# High-resolution measurements and simulations of the flow through a packed bed and its freeboard region

Wojciech Sadowski,<sup>1</sup> Mohammed Sayyari,<sup>1</sup> Francesca di Mare,<sup>1</sup> Christin Velten,<sup>2</sup> and Katharina Zähringer<sup>2</sup>

<sup>1</sup>*Chair of Thermal Turbomachines and Aeroengines, Ruhr-Universität Bochum, Universitätsstraße 150 D-44801 Bochum, Germany*

<sup>2</sup>*Lehrstuhl für Strömungsmechanik und Strömungstechnik, Otto-von-Guericke-Universität Magdeburg, 39106 Magdeburg, Germany*

(\*Electronic mail: [wojciech.sadowski@rub.de](mailto:wojciech.sadowski@rub.de))

(Dated: 17 November 2023)

The present study focuses on the assessment of the performance of a Finite Volume Method based, particle-resolved simulation approach to predict the flow through a model packed-bed consisting of 21 layers of spheres arranged in the body centred cubic packing. The unsteady flow developing in the freeboard is also considered. Two highly-resolved large eddy simulation were performed, for two Reynolds numbers, 300 and 500, based on the particle diameter, employing a polyhedral, boundary-conforming mesh. The geometry and the flow conditions are set to reproduce the flow conditions investigated in the experiment carried out by Velten and Zähringer<sup>1</sup> using Particle Image Velocimetry. The numerical results compare favourably with the measurements both inside and above the bed. The effect of differences arising between the physical and numerical configurations are thoroughly discussed alongside the impact of meshing strategy on the accuracy of the predictions.

## I. INTRODUCTION

Packed bed reactors represent a class of devices often used in chemical and process engineering, in which an assembly of particles is passed by a gas, usually ensuring appropriate mixing of species, introducing reactants or promoting processes such as drying or coating. The flow characteristics influence the phenomena occurring in these devices to a great extent. In particular, the effects of the intermittent coupling between the turbulent flow in the freeboard, a region above the particle assembly, and the interstitial flow between the particles has been seen to reach deep inside the packed bed<sup>2</sup>.

Numerical simulations can supply extremely valuable insight in the development of the flow in packed beds to various levels of accuracy, depending on the methodological approach. On one hand, the porous media approach provides a simplified, homogenised representation of the particle assembly, whereby the porosity, generally considered a scalar value, denotes the volume fraction occupied by the particles<sup>3</sup> and offers therefore an approximate description of the interstitial flow. On the other hand, in Particle Resolved Simulations (PRS),<sup>3-5</sup>, a detailed description of the passing flow and of the particles is pursued, requiring in particular appropriate turbulence closure. In the works by Shams *et al.*<sup>6,7,8,9,10</sup> exhaustive reviews of turbulence modelling strategies in packed beds are provided alongside a discussion of the nature of turbulence in the interstices by Jin *et al.*<sup>11</sup>, Uth *et al.*<sup>12</sup> as well as Rao and Jin<sup>13</sup>. Direct Numerical Simulation (DNS), entails the explicit resolution of all relevant length and time scales, ranging from those smaller the characteristic interstice dimensions and related to the turbulence length scale in the bed, to the overall dimension of the reactor, and are associated to prohibitively high computational costs<sup>3,14</sup>, above all in technologically relevant applications. Relaxing the spatial and temporal resolution requirements intrinsic of PRS is not a straightforward task. For example, an insufficient spatial resolution near the bed surface

could lead to an inaccurately predicted mean velocity in the whole region occupied by the solid phase and a greatly overestimated drag force induced by the particles<sup>15</sup>. In Breugem and Boersma<sup>16</sup> and Kuwata and Suga<sup>17</sup> DNS of flows over periodically repeating sets of obstacles with, respectively, a Finite Volume Method (FVM) and Lattice-Boltzmann-based solvers were presented. In the context of the finite-volume method, Shams *et al.*<sup>8,9</sup> conducted a DNS of a single cubic pebble bed configuration with heat transfer, revealing highly complex temperature and velocity distributions under turbulent conditions. Shams *et al.*<sup>18</sup> performed a Large Eddy Simulation (LES) of the flow through a randomly stacked pebble bed using FVM and a polyhedral boundary-conforming mesh. A major issue arises when performing FVM-based PRS from the necessity of resolving the small gaps between particles with a reasonable accuracy maintaining an acceptable mesh quality<sup>3</sup>. This problem is notoriously difficult to solve, and if untreated, can hinder the stability and accuracy of the computation<sup>19</sup>.

The Immersed Boundary Method (IBM) is often used in conjunction with FVM to simulate packed bed reactors, as it enables the use of simpler meshes, often of uniform size or refined by cell-splitting. The particle boundary is represented as virtually intersecting the fluid cells and its influence on the flow field is considered by applying a force field in the fluid domain. For example, Gorges *et al.*<sup>20</sup> simulated a packed bed using two implementations of the IBM with smooth and blocked-off particle boundaries. For similar reasons, the Lattice-Boltzmann Method (LBM) represents another useful alternative as showed by Neeraj *et al.*<sup>21</sup> who simulated the flow inside and over the surface of a packed bed. Reference experimental data for verification of such simulations is usually scarce due to the difficulty in accessing the interior of the packing. Hence, only limited validation of the numerical simulation is possible using generally global (macroscopic) quantities obtained from empirical correlations or very sparse and uncertain data. Wongkham *et al.*<sup>22</sup> (and references therein) used em-

irical correlations for the distribution of porosity near the wall and for the pressure drop along the packed-bed to validate the implementation of a novel IBM. Also, the experimental measurements of superficial velocity and porosity by Giese, Rottschäfer, and Vortmeyer<sup>23</sup> were used by Wehinger<sup>24</sup> to validate the FVM simulation approach for catalytic flow reactors. To the best of the authors' knowledge, studies validating numerical methods w.r.t. the accurate prediction of small-scale interstitial flow and the phenomena occurring in the freeboard are hardly attempted, mainly due to the scarcity of experimental data. However, recently data measured by Velten and Zähringer<sup>1</sup> in an experimental packed-bed configuration were used to assess both LBM- and IBM-based approaches, which have been shown to produce satisfactory results when it comes to the prediction of interstitial and freeboard flow<sup>20,21</sup>. Although the FVM approach remains a staple, both in industry and academia, its performance for PRS has not been assessed to the same extent. Experimental data on these kinds of flows can be generated by applying intrusive techniques such as hot wire anemometry<sup>25,26</sup> or endoscopic Particle Image Velocimetry (PIV)<sup>27</sup> to investigate the flow through the packing. The usual drawback of these methods lies in the fact that the insertion of the measurement device into the packed-bed disturbs the flow. Fortunately, other nonintrusive methods are also available. For example, tomographic techniques such as Magnetic Resonance Imaging (MRI)<sup>28–30</sup> or optical techniques such as planar PIV<sup>31–33</sup> or tomographic PIV<sup>34</sup> can be applied. While tomographic techniques are mainly limited to liquid flows and do not need optical accessibility, as it is the case for optical methods, the resolution in space and time is comparably low<sup>35,36</sup>. On the other hand, for optical techniques, transparent materials have to be used to allow for measurement access. When employing transparent packing material, however, distortion is introduced which, in the case of liquids, is usually handled by refractive index matching<sup>37</sup>. Unfortunately, this method is obviously not available for gaseous flows. Hence, most existing data on flow fields inside packed beds is based on liquids. Some approaches to overcome the issue in gases exist, either by additional post-processing, e.g., by calibration<sup>38</sup>, or a ray tracing based correction<sup>39,40</sup>. Nevertheless, standard PIV can also be applied to the gas flow in regions above the packed bed as well as small regions in the interior of the bed, specially if a regular arrangement, such as the body-centred cubic (BCC) packing, is investigated<sup>1</sup>.

In this paper, we conduct particle-resolved Large Eddy Simulations for two particle Reynolds numbers in a vertical packed bed configuration passed by a gas stream using Finite Volume Method. Gas velocity data gathered by PIV at the outlet and in the optically accessible interstices of a BCC packing<sup>1</sup> is used for validation and in order to facilitate the analysis of the computed results. The above mentioned optical obstructions limit the potential of the PIV data, however, the relatively idealised setup of a numerical simulation opens the door for extracting the results in regions inaccessible to current experimental measurement techniques. sentence be still here? The analysed geometry is based on the experimental set-up investigated by Velten and Zähringer<sup>1</sup>. Both the interstitial flow and the unsteady

velocity field above the surface of the bed is analysed. By directly comparing the predicted flow field to the measurements we demonstrate the capabilities and shortcomings of the classical boundary conforming FVM approach for PRS. We also discuss the potential effects of unavoidable discrepancies between the numerical and real geometrical arrangements on the prediction of the velocity field (see Section III). Finally, we analyse the computed results from the point of view of the influence of the wall channelling effects on the flow conditions inside the packing and the interactions between the flow in the freeboard and velocity inside the bed. The paper is structured as follows: first, the geometry and flow conditions are described in Section II, then, in Section III, the numerical setup is thoroughly discussed, followed by the description of the characteristics of the PIV equipment and positions of the measurement regions in Section IV. Finally, the results inside the packing and over the freeboard are described and discussed in Section V. Concluding remarks and an outlook of future research are summarised in Section VI.

## II. GEOMETRY AND FLOW CONDITIONS

The geometry of the experimental configuration (see Figure 1) consists of a bed built out of 21 alternating layers of spheres arranged in the BCC packing. The spheres are stacked in such a manner that the odd-numbered layers comprise nine spheres, and the even layers, referred to as weak layers, four. The sphere diameter is  $D_p = 0.04$  m. The theoretical porosity of the BCC packing is equal to  $\phi_t = 0.32$ .

The origin of the experimental coordinate system coincides with the baseplate's top surface as indicated in Figure 1b, which also depicts nine bearings (spherical insets) manufactured in the base plate to hold the lowest layer of spheres. This placement positions the centres of the spheres in the first layer at  $y = 0.475D_p$ . The plate is perforated with 312 gas flow inlet holes, with a diameter of  $D_h = 0.1D_p$  each.

The assembly is housed in a prismatic casing as shown in Figure 1a with a square cross-section. As the spheres are touching the casing walls, its size can be determined from the geometry of the BCC packing and is given as  $D_p(4\sqrt{3}/3 + 1) = 0.132$  m. The bed height with all 21 layers of spheres in place is 0.5 m as the centres of the spheres in the 21<sup>st</sup> layer are placed at  $y = 12D_p$ . The test chamber has a height of 0.92 m to reduce the influence of the environment on the freeboard.

For a direct comparison between the measurements and the numerical predictions differences between the ideal CFD model and the geometry in the experiment have to be considered. These differences occur due to manufacturing processing on the side of the experiment. For the test case considered in this paper, the spherical particles are glued together. The gluing process creates a bridge between the individual spheres, leading to a geometry deviating from the ideal BCC packing, increased vertical dimension of the whole particle assembly, and slightly increased size of the inter-particle gap in the interior of the bed. The PIV data presented in the paper has been appropriately shifted to

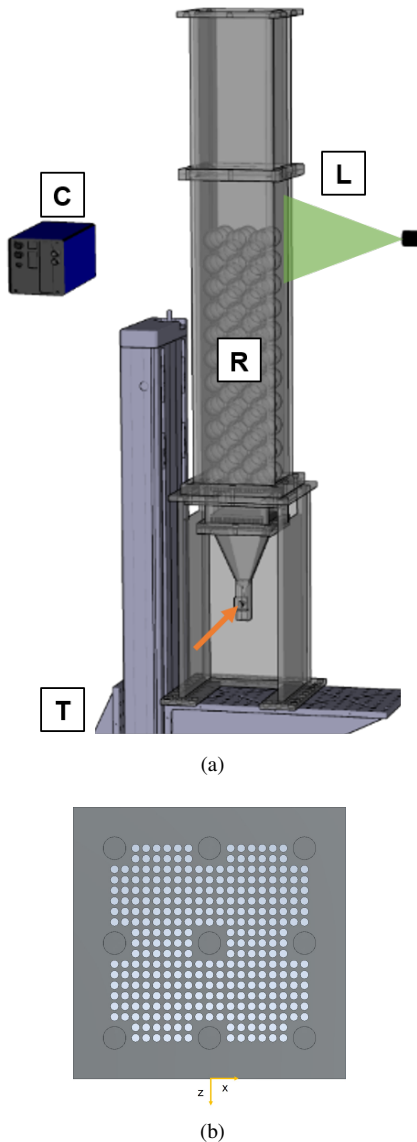


FIG. 1. Schematic of the geometry of the experimental configuration. In the top figure: the experimental test section (R) with the indicated position of the light sheet (L), the camera (C), and the traversing system (T). The packing houses 21 layers of spheres in a BCC structure. The lower picture presents the test section's baseplate with gas inlet holes (white circles) and bearings (black circles) housing the first layer of spheres. The axes shown in the picture represent the coordinate system of the PIV data, with the  $y = 0$  plane coincident with the top surface of the baseplate and the  $y$  axis directed upwards.

account for this change in size. However, these features could not be exactly reproduced in the numerical model, which, therefore, is a high-fidelity but nevertheless approximate representation of the experimental configuration.

The present work considers two cases corresponding to two experimental data sets, characterised by Reynolds number based on the particle size  $Re_p = 300$  and 500. The Reynolds number is defined here as

$$Re_p = \frac{\rho D_p \langle v \rangle}{\mu}, \quad (1)$$

where  $\mu = 1.882 \times 10^{-5}$  Pas is the air viscosity at the ambient conditions (pressure of 1 bar, the temperature of 20 °C) and  $\langle v \rangle$  is the intrinsic average of the velocity of the gas flowing through the packing<sup>41</sup>.

The intrinsic average of velocity employed in Equation (1) can be readily obtained from the volumetric flow rate measured in the experiments as  $\phi_t \langle v \rangle = Q/A$ , where  $Q$  is the flow rate and  $A$  is the cross-section of the packing. The flow rates for  $Re_p = 300$  and 500 are given as 38.2 and 63.6 l min<sup>-1</sup> respectively.

### III. MATHEMATICAL MODEL

The simulations presented in the study are performed with the pimpleFoam solver from OpenFOAM, a FVM-based CFD package (version v2306). For a thorough description of numerical methods used in OpenFOAM, the reader is referred to the works by Jasak<sup>42</sup> and Moukalled, Mangani, and Darwish<sup>43</sup>. The solver is based on the low-Mach formulation of the Navier–Stokes equations

$$\frac{\partial u_i}{\partial t} + u_j \frac{\partial u_i}{\partial x_j} = -\frac{\partial}{\partial x_i} \left( \frac{p}{\rho} \right) + \nu \frac{\partial^2 u_i}{\partial x_j \partial x_j}, \quad (2)$$

$$\frac{\partial u_i}{\partial x_i} = 0, \quad (3)$$

where  $\mathbf{u}$  is the velocity,  $p$  pressure and  $\nu = \mu/\rho$  is the kinematic viscosity. In their work, Gorges *et al.*<sup>20</sup> conducted computations of the same configuration without a sub-grid scale model and Komen *et al.*<sup>44</sup> successfully employed a similar setup. To assess the sensitivity of the predictions presented in this paper to the turbulence model, precursory calculations were performed with and without the sub-grid scale model and the influence of the latter on the results was indeed found to be negligible for the mesh resolution and Reynolds numbers considered. Hence, we opted not to employ any turbulence closure for the presented computations. The computational domain is shown schematically in Figure 2a. The coordinate system of the numerical domain is defined so that it coincides with the one used to describe the experimental rig.

To simplify the meshing process, the baseplate, along with the honeycomb structure, have been replaced with an idealised planar inlet placed at  $y = -D_p$  (see Figure 2). The lack of the baseplate in the meshed geometry allows for high-quality cells near the bottom of the 1<sup>st</sup> layer of spheres, where highly skewed cells are generated near the bearings, which could influence the stability of the computation.

Following the observations made by Velten and Zähringer<sup>1</sup> and Neeraj *et al.*<sup>21</sup>, in the studied configuration, the flow in the interstices and above the bed seems to be independent of the bed height, provided the particle assembly is made up of more than 19 layers. This effectively rules out any influence of the flow conditions at the inlet on the unsteady flow at the freeboard, which justifies the simplification of inlet geometry.

The section of the structure downstream of the spheres has also been extended to minimise the influence of the outlet condition on the unsteady flow in the freeboard.

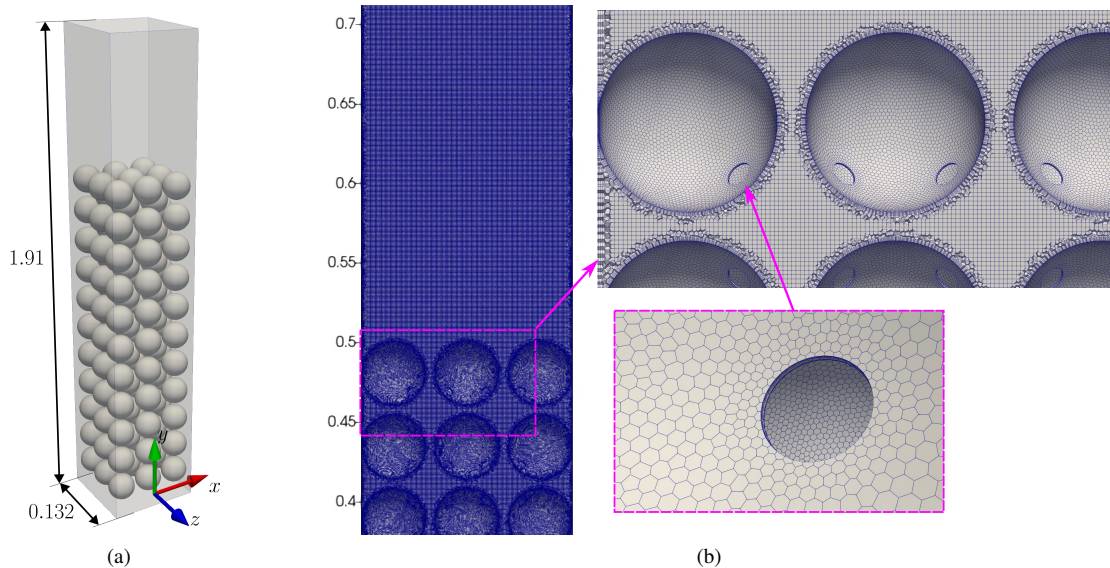


FIG. 2. Left figure: schematic of the computational domain (the height dimension is not to scale). Right picture: computational mesh clipped at the symmetry plane perpendicular to the  $z$  axis. The zoomed-in view shows the mesh around the simplified contact point between spheres in two different layers.

Hence, in the computations, the domain has dimensions of  $0.132 \times 0.132 \times 1.91$  m.

In the context of particle-resolved simulations on boundary-conforming meshes, some geometry simplifications are often required to avoid numerical issues and time-step limitations caused by small and often malformed cells generated by the meshing algorithm at the contact point of two particles. Dixon and Partopour<sup>3</sup> and references therein recommend the so-called *bridges* method, which is based on connecting the abutting geometries with a cylindrical solid volume. The diameter of the cylinder should not be greater than 20 % of the particle diameter. This approach has been used in the current study for the contact points between the spheres themselves and the areas between the spheres and the casing walls. It also represents well the fact that spheres have been glued. The cylinder diameter used for the bridges was set to  $0.015D_p$ . Figure 2b shows the mesh around the simplified geometry.

Typically, when conducting scale-resolving simulations, the preferred meshing strategy consists of preparing a high-quality, smooth, preferably structured mesh with hexahedral elements. However, such an approach is challenging to implement in complex geometries like the one studied in the present work and, if used, would lead to exceedingly high cell counts. Instead, a hybrid polyhexacore mesh was generated using the Ansys Fluent meshing module<sup>45</sup>, due to the ability of the meshing algorithm to generate unstructured polyhedral mesh near the solid boundaries, while the core flow is still resolved on a uniform hexahedral grid. The resulting mesh is characterised by low non-orthogonality and skewness, which makes the computational method more robust. The mesh is visible in Figure 2b and consists of 19 M cells, of which around 51 % are characterised by polyhedral shapes. The statistics of the mesh are listed in Table I.

Polyhedral meshes were previously successfully used

TABLE I. Statistics of the mesh employed in the computations, face non-orthogonality, cell skewness and non-dimensional wall spacing computed for each simulation.

Non-ortho.		Skewness		$y^+$				$x^+/z^+$			
Avg.	Max	Avg.	Max	$Re_p = 300$		500		300		500	
				Avg.	Max	Avg.	Max	Avg.	Max	Avg.	Max
4.5°	58.9°	0.1	3.7	0.1	0.6	0.17	0.75	1.5	9.5	2.15	11.5

for scale-resolving simulations of packed beds<sup>6,8,9,18</sup>. Their performance in OpenFOAM for scale-resolving simulations, along with other mesh types, has also been rigorously tested in a fully turbulent pipe flow<sup>46</sup>, showing a satisfactorily agreement with results generated by highly accurate spectral codes.

The cubical cells in the core flow have a size of approximately  $D_p/40$ , which should provide sufficient resolution for the selected simulation, considering that Gorges *et al.*<sup>20</sup> were able to adequately resolve most of the mean features of the flow using IBM and a grid with spacing equal to  $D_p/32$ . To resolve the contact regions appropriately, the cell size has been set to  $D_p/200$  in these regions. The boundary layer is resolved with 4 layers of prismatic cells with the expansion rate of 1.2. The region of the mesh above the outlet of the experimental rig  $y > 23D_p = 0.92$  m has been meshed by extruding the top boundary, generating prismatic cells with a polyhedral cross-section. The mesh has been coarsened in the streamwise direction  $y$  to generate a sponge layer the outlet and thus further prevent back propagation of disturbances upstream.

Both simulations were performed using a second-order central scheme for the convective terms along with second-order accurate interpolation schemes. For time integration, a second-order implicit backward scheme was used. The PISO (Pressure-Implicit Splitting Operator) algorithm<sup>47</sup>

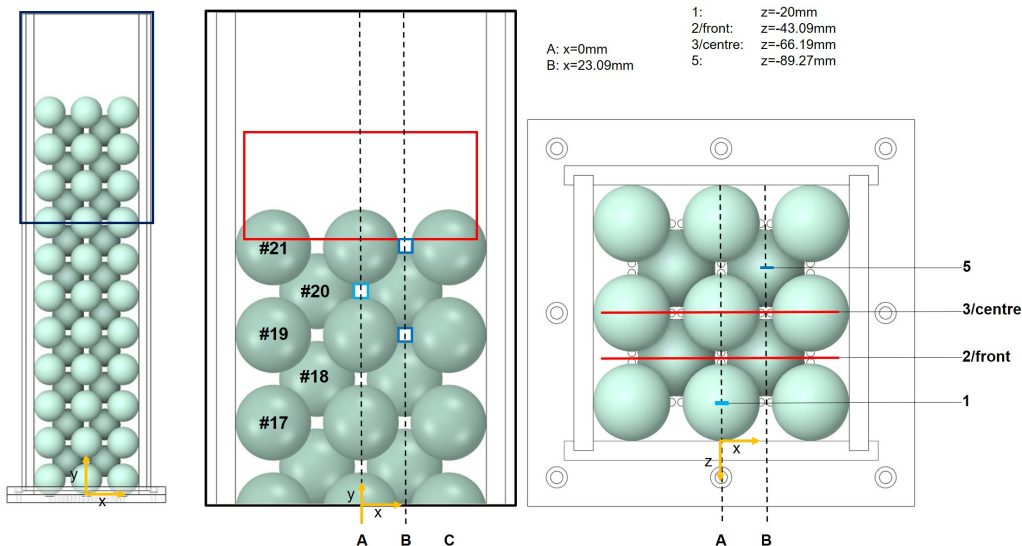


FIG. 3. Front view of the packed bed configuration with 21 layers of spheres in a BCC packing (left). The black rectangle marks the zoomed-in region into the layers of interest (17-21), visible in the centre. In this view, the measurement region above the bed is marked as a red rectangle. The small blue squares locate the flow data inside the packed bed. Here, the dark blue marks the regions of interest for the full layers (19 and 21) and the light blue represents the interstices in layer 20. In the top view (right), red lines show the  $z$  coordinate of the four measurement planes: 1, 2 (or front plane), 3 (or centre plane) and plane 5.

was adopted with five corrector loops and three sub-iterations to correct for non-orthogonality. In the case of  $Re_p = 300$ , the time step was chosen to be  $\Delta t = 0.0008$  s, whereas for  $Re_p = 500$  it was equal to  $\Delta t = 0.0005$  s, resulting in a CFL number smaller than 0.8 in both cases.

Uniform velocity was prescribed as an inlet condition with a value computed from the volumetric flow rates measured during the experiments. The reference value for pressure has been prescribed at the outlet, while, for velocity, a surface normal gradient equal to zero has been assumed. The surfaces of the bridging cylinders are treated as walls with no-slip conditions for velocity.

With the flow through time defined using the size of the packing  $L_z = 23 D_p = 0.92$  m and the intrinsic velocity in the packing:  $T_{FFT} = L_z / \langle v \rangle$ , to allow for a full development of the flow field above the bed before the collection of the statistics, both simulations were run for  $4.5 T_{FFT}$  and  $7 T_{FFT}$ , for  $Re_p = 300$  and  $500$  respectively. Following that, results for  $Re_p = 300$  and  $Re_p = 500$  were ensemble-averaged for  $37 T_{FFT}$  and  $83.5 T_{FFT}$ . These values correspond to around 300 s and 405 s of simulated flow time.

#### IV. PIV SETUP

The air flow entering the rig is regulated by a Bronkhorst Mass-Stream Controller (D-6371; 5001/min air) and seeded with Di-Ethyl-Hexyl-Sebacat (DEHS) particles provided by a nebulizer. A Quantel Q-smart Twins 850 Nd:YAG PIV-laser and a light sheet optic is used to create a laser light sheet and illuminate the tracer particles in the plane of interest, which can be reached by moving the packing on the 3D traversing system (see Figure 1a). For measurements above the bed a LaVision Imager LX 8M

camera equipped with a Nikon AF Nikkor 35 mm f/2D lens was used. The interstitial flow was captured with a LaVision Imager Intense camera equipped with a Nikon Micro-Nikkor 105 mm f/2.8D lens.

Image recording took place with a frequency of 2.5 Hz and the recording time of 120 s and 400 s (300 and 1000 recorded double frame images) for  $Re_p = 300$  and  $500$  respectively. The double frame images are evaluated by a cross correlation method using Davis 8.4.

The measurement regions for the data used in this work are illustrated in Figure 3. The region above the bed is investigated in two different planes: front ( $z = -43.09$  mm) and centre ( $z = -66.19$  mm) marked by a red rectangle in the front view (middle part of Figure 3) and red lines in the top view (on the right). For the interstitial flow, the data is acquired for layers 19-21 and the positions are marked in blue. For better comparability to the original data by Velten and Zähringer<sup>1</sup>, the same convention is used to name the regions of interest: a letter denoting the  $x$  coordinate (“A” or “B” from the centre part of Figure 3) followed by the plane number a backslash and the layer number, e.g., A1/20 for the light blue square in the middle part of Figure 3.

#### V. RESULTS

##### A. General description of the flow field

An impression of the computed flow field is provided in Figure 4, where the mean velocity distribution is presented on the front plane, the symmetry plane of the geometry perpendicular to the  $x$  axis and the slice at  $y = 13 D_p$ . The velocity distribution in the interstices, discussed at length

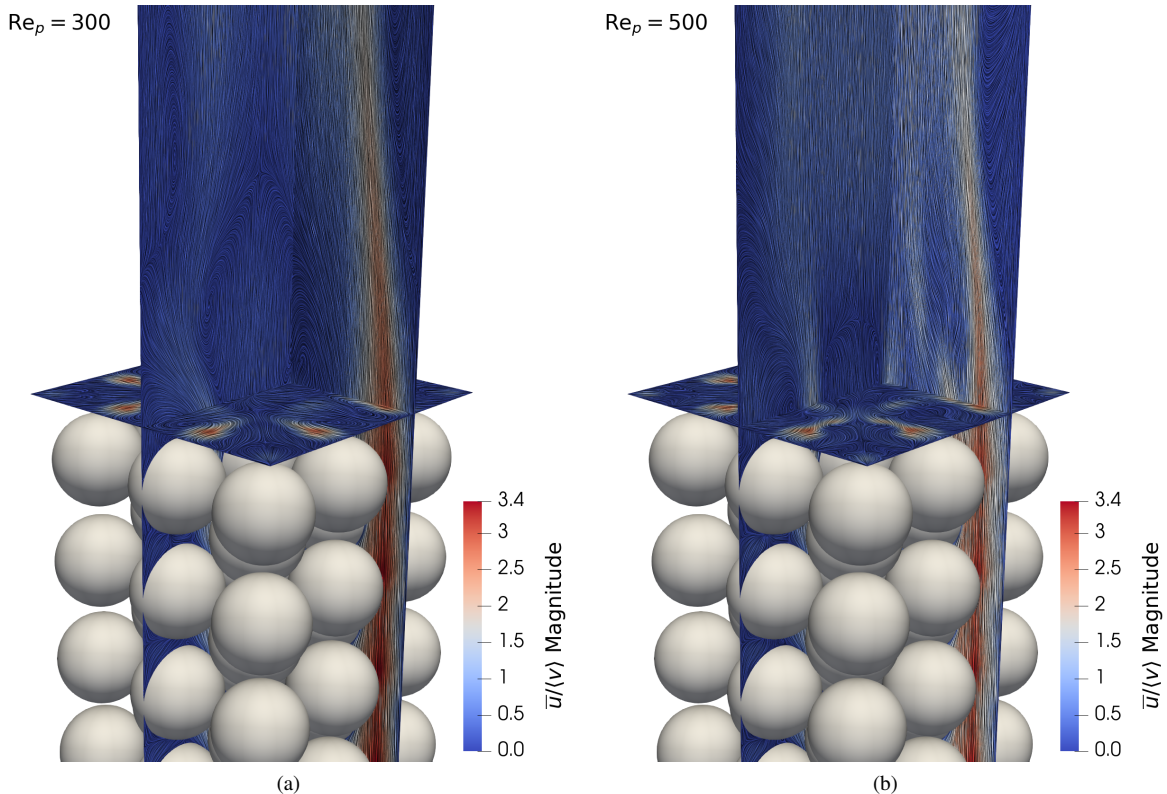


FIG. 4. Overview the flow field inside and over the studied packed-bed reactor at  $Re_p = 300$  (left) and  $Re_p = 500$  (right). Both pictures illustrate the normalised ensemble-averaged velocity magnitude along with the streamlines visualised by Line Integral Convolution method.

in Section VB, is characterised by a strong dominance of the wall-channelled flow. The presence of the weak layers, i.e., the lack of the spheres near the walls in the even layers, enables an unobstructed flow, which has a strong influence on the velocity field downstream in the freeboard.

The fluid exits the packed with non-uniform velocity; fluid in the centre of the geometry is noticeably slower than the wall-channelled fluid, resulting in the presence of large recirculation regions over the surface of the packing (see Section VC for detailed description). Additionally, the jets of fluid issuing from the near-wall interstices are directed towards the centre of the packing. This process is visibly faster for the higher  $Re_p$ , due to the presence of secondary jets which contribute to a redistribution of the momentum and thus tend to homogenise the upwards flow. Whilst essentially stationary conditions prevail inside the bed, the freeboard flow is dominated by low-frequency swirling and flapping motions, as also pointed out by Neeraj *et al.*<sup>21</sup>. The regions of unsteady flow, discussed in Section VD are located around the jets, however the onset of fluctuating motion can be identified below the crests of the topmost spheres.

## B. Flow inside the packed-bed

Focusing first on the interstitial flow, in Figures 5 and 7, we compare the measured and simulated velocity fields inside the bed, in the interstices near the wall. Additionally,

to further illustrate the features of the flow, in Figure 6, we discuss the properties of the velocity field around the measurement sections (the regions captured by PIV are also indicated in the same figure).

Figure 5 shows the recirculation region near the surface

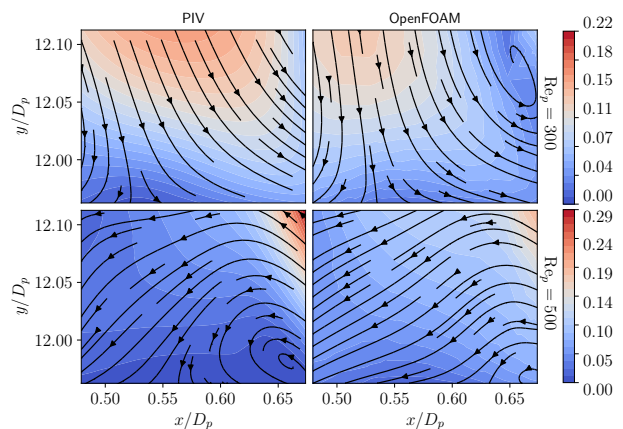


FIG. 5. The magnitude of normalised ensemble-averaged velocity  $|\bar{\mathbf{u}}/\langle v \rangle|$ : a comparison between the PIV measurements (left) and the results of the simulation (right) for  $Re_p = 300$  (top row) and 500 (bottom) in region B5/21 from Figure 3 (see also annotations in Figure 6). Arrows denote streamlines of the velocity field. Mind the different colour bars for different  $Re_p$ .

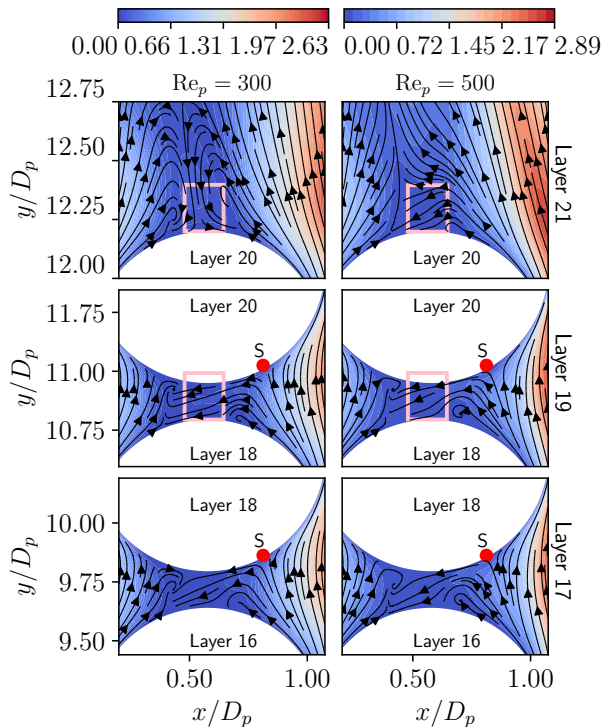


FIG. 6. The magnitude of normalised velocity  $|\overline{\mathbf{u}}/\langle v \rangle|$  in the interstices of the 17<sup>th</sup>, 19<sup>th</sup> and 21<sup>st</sup> layer for  $Re_p = 300$  (left) and 500 (right), plotted at the plane 5 (see Figure 3). Mind the different colour bars for different  $Re_p$ . Arrows denote streamlines of the velocity field. Label “S” indicates schematically the position of the stagnation point discussed in Section V B. The boxes show the regions measured by PIV, B5/21 and B5/19.

of the bed above the spheres in the 20<sup>th</sup> layer for both  $Re_p$ . The most pronounced feature of the flow in the neighbouring area is the fast-moving jet on the right hand side, accelerated in the openings between the packing and the wall, and released into the freeboard via the interstices of the 21<sup>st</sup> layer. These fast-moving jets, for both  $Re_p$  are visible in Figure 6 on the right of each plot. As indicated in the figure, the PIV measurement regions were positioned to the left of one of the wall-adjacent interstices, i.e. in the areas exhibiting high flow velocity due to the wall-channelling effects. This in turn leads to the presence of a large recirculation region above the spheres in 20<sup>th</sup> layer visible in the PIV and simulation data in Figure 5.

For  $Re_p = 300$ , the measurement section is dominated by a downwards directed flow, which slows down while approaching the surface of the sphere (located just below the measurement window). The bulk of the flow is redirected to the right, where it joins the fluid accelerated next to the wall. Due to the presence of the faster flow near the wall, the velocity field is visibly asymmetric with respect to the sphere positioned below the measurement section, centered at  $x = 0.57725D_p$ . Thus, the reattachment point at the surface of the sphere is visibly skewed to the left side of the observed region.

The main difference between the simulated and measured flow is the presence of a vortex in the simulation data

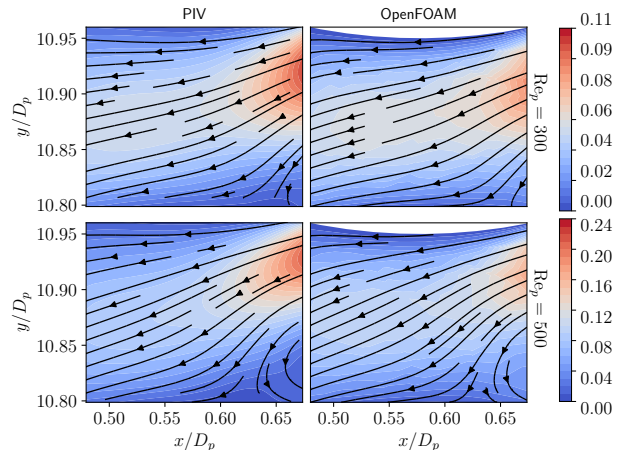


FIG. 7. The magnitude of normalised ensemble-averaged velocity  $|\overline{\mathbf{u}}/\langle v \rangle|$ : a comparison between the PIV measurements (left) and the results of the simulation (right) for  $Re_p = 300$  (top row) and 500 (bottom) in region B5/19 from Figure 3 (see also annotations in Figure 6). Arrows denote streamlines of the velocity field. Mind the different colour bars for different  $Re_p$ .

for  $Re_p = 300$  on the top-right part of Figure 5. This feature is not visible in the PIV measurements. It can be argued that the recirculation region as a whole is narrower than in the experimental measurement of the flow field. However, the overall character of the flow is reproduced well in the simulated results.

On the other hand, in the case of  $Re_p = 500$ , the comparison between the predicted velocity field and the PIV measurement is even more satisfactory (Figure 5). As for lower  $Re_p$ , the flow separates from the sphere in the 20<sup>th</sup> layer; however, the recirculation region is much smaller, with the reattachment occurring right of the centre of the measurement section. Further, the flow in this case is mainly directed downwards and towards the centre of the structure, which seems to drive a faster reattachment of the separation bubble. Similarly to the  $Re_p = 300$  results, the predicted separated region is noticeably smaller than in the PIV measurement.

Overall, looking at Figure 6, for  $Re_p = 300$ , the recirculation region above the 20<sup>th</sup> layer appears to be stretched in the vertical direction due to the limited space between the spheres in 21<sup>st</sup> layer. Yet, the velocity field of the  $Re_p = 500$  case is visibly more complex. Instead of forming a pair of vortices, the flow from the near-wall jets impinges on the fluid coming from the left, forcing a closer reattachment of both recirculation regions. Nevertheless, both flows share many similarities, with the recirculation regions skewed towards the centre of the studied geometry and the overall character of the flow field being clearly dominated by the behaviour near the walls.

Figure 7 shows the flow conditions directly below the previous measurement window, at the height of the 19<sup>th</sup> layer of spheres. Here, simulation results are also in very close agreement with the experimentally measured velocity field. For both Reynolds numbers, the overall character of the flow is adequately reproduced in the simulated data.

For each even layer, the flow next to the walls impinges onto the surface of the higher spheres due to the expansion of the interstitial space next to the wall (layers 17 and 19 at the right sides of the colour maps in Figure 6, stagnation point schematically indicated by the letter S). Part of the fluid is then diverted into the narrow gap between the spheres in the odd layers. This faster moving swath of fluid enters the measurement area in the top-right corner for both  $Re_p$  numbers. This results in the flow being directed towards the centre of the geometry and the presence of a recirculation and reattachment in the bottom part of the region of interest. The flow reattaches on the sphere in the next layer and part of the fluid returns to the “channel” near the wall. For  $Re_p = 500$ , faster fluid is transported deeper towards the centre of the structure, increasing the size of the separation bubble w.r.t. lower  $Re_p$ . Inspection of the velocity field on the other side of the area captured by the PIV data and illustrated in Figure 6 also reveals a complex behaviour. The fluid channelled between the spheres in even layers mixes with the vertical flow convected through the middle of the packing, resulting in a stronger recirculating flow.

Figure 6 shows clearly how the proximity of the bed surface influences the interstitial flow field in the top three odd layers. In between the layers 16<sup>th</sup> and 18<sup>th</sup>, as well as 18<sup>th</sup> and 20<sup>th</sup>, the velocity fields remain remarkably similar. On the other hand, the differences in the flow field in the interstices of the 19<sup>th</sup> and 21<sup>st</sup> layers are much more pronounced. This can be explained by the fact that the flow is able to separate effectively with no constraints from the 20<sup>th</sup> layer of spheres.

This seems to suggest that the conditions near the surface of the packing have a strong influence on the flow inside the last layer of spheres, but not further downwards, which appears to be mostly driven by the geometry and arrangement of the particles. For the BCC packing under the investigated Reynolds numbers, the main features of the flow in the freeboard are therefore mostly determined by the arrangement of the particles in the top two layers. Additionally, when no backflow from the freeboard into the bed is present, the flow conditions deviate from the ones inside the packed bed only near the two topmost layers.

Figure 8 illustrates the flow around the  $x = 0$  symmetry plane of the structure at the height of the 20<sup>th</sup> layer. In this region, the flow field should be symmetric; this property is, however, not fully captured in the measured data. Based on the simulation results, the velocity should be characterised by two recirculation zones, driven by the mean streamwise flow through the packing, meeting in the middle of the region, i.e. around  $x = 0$ . In the experimental results, for both Reynolds numbers, both recirculation zones seem to be shifted towards the negative values of  $x$ . This effect is more pronounced for the higher  $Re_p$ , as the whole measurement region seems dominated by the flow in the left direction. This behaviour is potentially caused by the unavoidable inaccuracies resulting from assembling and gluing the spheres in the packed bed.

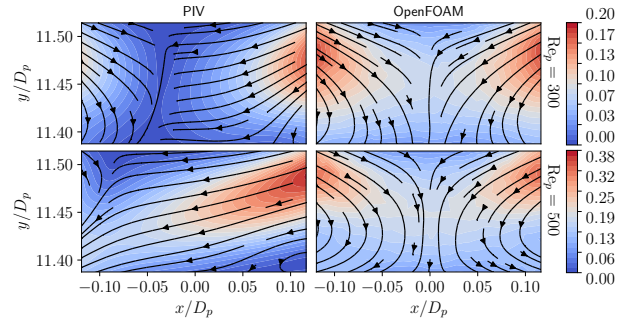


FIG. 8. The magnitude of normalised ensemble-averaged velocity  $|\bar{u}/\langle v \rangle|$ : a comparison between the PIV measurements (left) and the results of the simulation (right) for  $Re_p = 300$  (top row) and 500 (bottom) in region A1/20 from Figure 3. Arrows denote streamlines of the velocity field. Mind the different colour bars for different  $Re_p$ .

### C. Flow above the bed

The ensemble-averaged, streamwise component of the velocity over the bed surface, on the **front** and **centre** measurement planes, is presented in Figures 9 and 10 respectively. Due to the strong wall-channelling effects, for both  $Re_p$  the flow at the front plane is dominated by two jets issuing from the bed with velocities which result to be 3–4 times higher than the theoretical intrinsic average velocity  $\langle v \rangle$ . The flow originating from the bed through the gap in the centre of the freeboard (around  $x = 0$ ) is much slower, with simulation results indicating maximum velocity of around  $1.5\langle v \rangle$ .

For the lower  $Re_p$ , the middle part of the PIV measurement section is characterised by a backflow. Two recirculation regions are visible forcing the fluid flowing out of the bed in the centre of the freeboard to join the flow in the jets. This behaviour cannot be observed in the simulated results. Qualitatively, the character of the flow field is predicted accurately by the simulations, although the computed jets are noticeably wider and more diffused. This in turn, seems to reduce the recirculation regions to a much smaller vortex located over the centre of the packing, where the fluid ejected from both wall-adjacent interstice and the one at the centre get mixed.

A similar flow structure can be observed in PIV data in the case of  $Re_p = 500$ . Two regions of fluid accelerated near the wall are again the most important feature of the velocity field. Here, the simulation results are in a very good agreement with the measured flow field. Additionally, both measurement and simulation data indicate the presence of two additional diagonal jets. The jets have a higher velocity near the bed in the simulations, however, they dissipate more quickly. Additionally, no recirculation is visible between each pair of the jets. Based on the computed velocity field, the additional jets also originate from the interstices adjacent to the wall. The presence of these diagonal jets seems to redistribute the velocity more evenly, facilitating the flow leaving the bed in the middle of the packing and reducing the size of recirculating regions

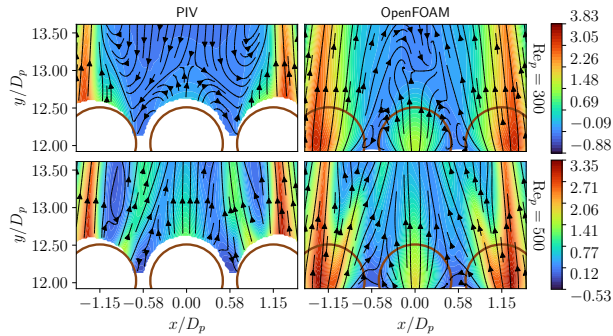


FIG. 9. The magnitude of vertical component of ensemble-averaged velocity  $\bar{v}/\langle v \rangle$ : a comparison between the PIV measurements (left) and the results of the simulation (right) for  $Re_p = 300$  (top row) and 500 (bottom) above the bed surface at the front plane (see Figure 3). Arrows denote streamlines of the velocity field. Mind the different colour bars for different  $Re_p$ . The positions of spheres in 21<sup>st</sup> layer is annotated on each graph. In case of PIV measurements, white colour denotes area where the velocity was not captured by the camera.

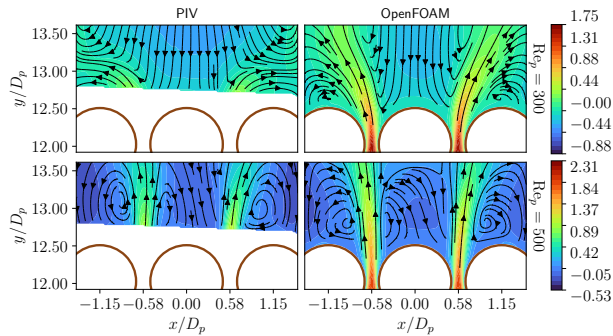


FIG. 10. The magnitude of vertical component of ensemble-averaged velocity  $\bar{v}/\langle v \rangle$ : a comparison between the PIV measurements (left) and the results of the simulation (right) for  $Re_p = 300$  (top row) and 500 (bottom) above the bed surface at the centre plane (see Figure 3). Arrows denote streamlines of the velocity field. Mind the different colour bars for different  $Re_p$ . The positions of spheres in 21<sup>st</sup> layer is annotated on each graph. In case of PIV measurements, white colour denotes area where the velocity was not captured by the camera.

of the fluid.

For both  $Re_p$ , the flow at the centre plane, visible in Figure 10, is characterised by the presence of two streams ejected from the gap between the topmost layer of spheres. For  $Re_p = 300$ , according to the PIV results, the ejected fluid is quickly redistributed towards the sides of the freeboard, and the jets are mostly diffused below  $y = 0.52 \text{ m} = 13D_p$ . Above, in the centre, a region of downwards directed velocity field is measured, creating two recirculation regions above the jets. Although the computed velocity field is in close agreement with the measurements, higher velocities characterise the jets in the numerical predictions, which, in turn, allows them to exist beyond  $y = 13D_p$ . Nevertheless, they behave qualitatively in a similar fashion as observed in the experiments, as they are also di-

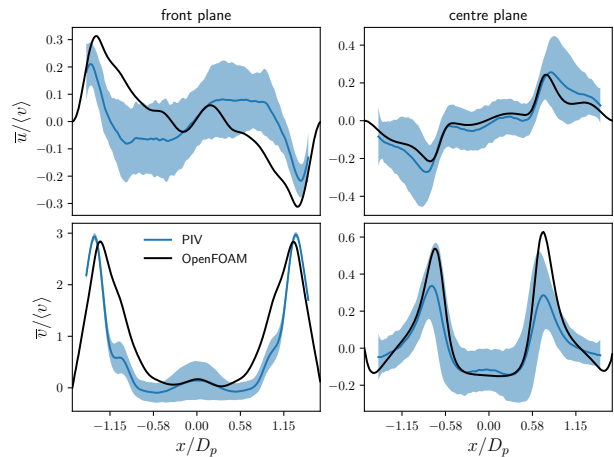


FIG. 11. Comparison of the ensemble-averaged horizontal (top) and vertical (bottom) velocity components for  $Re_p = 300$ , at the front (left) and centre planes (right), plotted at  $y = 12.8D_p$ . The blue band denotes the range of values separated from the measured data by two standard deviations denoting the 95% confidence interval.

rected towards the walls. As the jets remain closer to the centre longer, the backflow region above the centre of the packing is smaller and characterised by a lower velocity. Simulation results also reveal the presence of two recirculation regions above the surfaces of the spheres near the walls.

As the inertial effects get stronger with higher Reynolds number, at  $Re_p = 500$  the ejected fluid gets convected upwards instead of being quickly directed towards the wall, for both experiment and simulation. This leads to the presence of two big recirculation regions above the two off-center spheres and relatively strong downwards flow in the middle of the captured region.

A small break in the symmetry of the measured velocity fields can be observed, albeit not to a large extent: both jets are slightly angled towards the right side of the freeboard. Similarly to the conditions inside the bed (Figure 8), this was probably caused by the already discussed slight asymmetries of the experimental rig and packing itself.

The shape of the jets are predicted much better for the higher  $Re_p$ , although the computation still overpredicts the velocity in the core of each jet. Simulation results are also not entirely symmetrical, with the middle section in between the jets dominated by a diagonal downwards flow. The recirculation regions resulting from the presence of the jets reattach at the surface of the spheres.

Figure 11 presents a quantitative comparison of the mean velocity components at the front and centre plane at  $Re_p = 300$ , sampled at  $y = 0.512 \text{ m} = 12.8D_p$  from both the PIV data and simulation results. The PIV results include a confidence interval of two standard deviations, representing the 95% confidence level visible as the blue band on the graphs. Focusing first on the ensemble-averaged streamwise velocity,  $\bar{v}$ , at the front plane, the jets predicted in the simulation are noticeably wider than their measured counterparts. The peaks of maximum velocity are also

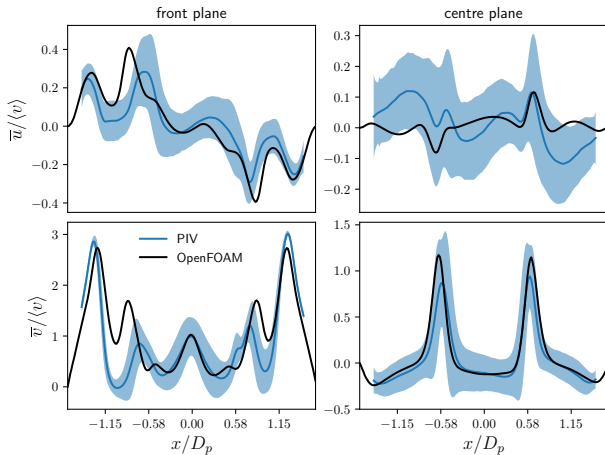


FIG. 12. Comparison of the ensemble-averaged horizontal (top) and vertical (bottom) velocity components for  $Re_p = 500$ , at the front (left) and centre planes (right), plotted at  $y = 12.8D_p$ . The blue band denotes the range of values separated from the measured data by two standard deviations denoting the 95% confidence interval.

slightly shifted towards the middle of the freeboard. The PIV results also indicate the presence of two smaller peaks in the streamwise velocity around  $x/D_p = \pm 1$ , which are potentially the weaker counterparts of the diagonal jets present in the  $Re_p = 500$  simulation.

The magnitude of the horizontal velocity component  $\bar{u}$  is also overpredicted in the same area, so that the jets predicted by the simulations are wider due to an increased convection towards the centre of the freeboard w.r.t. the PIV data set. Nevertheless,  $\bar{u}$  shows a trend similar to the measured data, with the maxima of horizontal velocity located near the wall. It has also to be kept in mind, that the fluctuations of the horizontal velocity component are much stronger than for the vertical one, which can be seen from the standard deviation of the experiments. This also influences the mean values obtained in both experiment and simulation.

The horizontal velocity component is in an excellent agreement with the experimental results at the centre plane (right column of Figure 11). The line plots of PIV also show a stronger flow towards the walls then computed, identified by the higher velocity magnitude in the near-wall regions. The streamwise velocity at the centre plane measured by PIV is also slightly asymmetric for this lower Reynolds number. The maxima of vertical velocity are significantly overpredicted however the overall shape and position of the jets is rendered in a similar way to the PIV results. The recirculation regions near the walls are also more pronounced indicating bigger recirculation regions in the simulations.

The same comparison was performed for the higher Reynolds number and is presented in Figure 12. Focusing first on the streamwise velocity at the front plane, the flow structure is visibly more complex than in the  $Re_p = 300$  case. The velocity profile is characterised by the presence of five peaks, corresponding to the five jets: two ejected

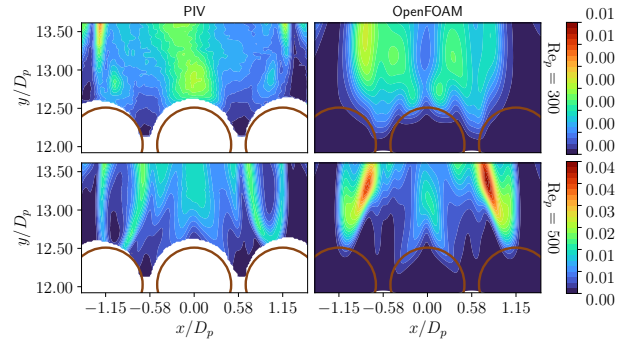


FIG. 13. The normalised TKE  $k/\langle v \rangle^2$ : a comparison between the PIV measurements (left) and the results of the simulation (right) for  $Re_p = 300$  (top row) and  $500$  (bottom) above the bed surface at the front plane (see Figure 3). Mind the different colour bars for different  $Re_p$ . The positions of spheres in 21<sup>st</sup> layer is annotated on each graph. In case of PIV measurements, white colour denotes area where the velocity was not captured by the camera.

from the interstices near the walls as at  $Re_p = 300$ , two smaller ones directed towards the middle of the freeboard and the fluid exiting the packed-bed in the centre (see the discussion related to Figure 9). In this case, the simulation results predict the position and shape of the two bigger jets much better than in the case of  $Re_p = 300$ . Similarly to the low Reynolds number results, the velocity in the middle is predicted to a very high degree of accuracy. The position of the secondary jets mentioned above is visibly shifted towards the sides of the freeboard, with much higher velocity then measured experimentally, which aligns with the observations based on Figure 9. An analogous behaviour can be observed by examining the horizontal velocity component: simulation results match the experimental data very well, although the maxima of simulated velocity are also shifted towards the walls.

The predicted streamwise velocity at the centre plane shows a very good agreement with the experimental data with a slight overestimation of the maximum velocity inside the jets and the recirculation regions near the walls are reproduced with an excellent accuracy. The velocity prediction does not match well the experimental data for the horizontal component, although most of the profiles still falls within the 95% confidence interval. Computation predicts virtually no horizontal flow near the walls whereas the PIV data indicates that the flow is directed towards the center of the bed.

#### D. Analysis of unsteady flow over the bed

As the flow detaches from the spheres in the topmost layer, it display a higher degree of unsteadiness. In the PIV measurement data only two components of the velocity in the plane illuminated by the laser sheet are available, therefore the turbulent kinetic energy (TKE) is computed in an approximated way as

$$k_{\text{PIV}} = \frac{3}{4} (\overline{u'u'} + \overline{v'v'}). \quad (4)$$

This approximation is based on the assumption of isotropy, i.e., the third component of normal fluctuations contains similar turbulent contribution as the other two<sup>48</sup>. Since in the simulations all three components of velocity are resolved, the TKE can be computed according to the theoretical definition<sup>49</sup>:

$$k = \frac{1}{2} \overline{u_i' u_i'}. \quad (5)$$

Figure 13 illustrates the distribution of the turbulent kinetic energy (TKE) at the front plane above the bed. Data from both the PIV measurements and simulations is presented, at both  $Re_p$  numbers. For centre plane the same comparison is visible in Figure 14.

At the front plane, the simulation results for  $Re_p = 300$  are in qualitative agreement with the data measured using PIV. There are, however, significant differences. PIV indicates the presence of two elongated highly unsteady regions near the walls, at the height of  $y = 13.5D_p$ . Furthermore, over the surface of the bed, around  $x = \pm 1.15D_p$ , the fluid exiting the packing at the middle of the front plane and joining the flow near the walls (see Figure 9) seem to create an additional pair of small areas of unsteady flow. The middle of the freeboard is also dominated by a region of increased TKE which gets progressively shifted to the left side. These rather separate structures are not predicted by the PRS, potentially due to the overly diffused jets. Instead, the TKE seems to be located in two symmetric spots above the bed, generated both by the influence of the shear layer due to the presence of the jets and the oscillating flow in the middle of the front plane. The latter feature of the PIV data is satisfyingly reproduced by the simulation results, with two regions of increased TKE near the surface of the bed in the centre of the front plane. A conclusion on the isotropy and nature of the turbulence cannot be drawn based on the evidence of the comparison presented in the paper and further investigations are required.

For the higher Reynolds number, PIV data illustrates five distinct areas of high TKE, corresponding to the five regions occupied by faster flow and resulting recirculation regions, visible in Figures 9 and 12. The TKE computed from the numerical flow fields is in a much closer agreement to the experimental measurement than for the lower  $Re_p$ . The unsteady region in the middle of the freeboard is clearly visible in the computed field. Instead of the narrow regions of high TKE visible in the measured data at the sides of the freeboard, the simulation predicts more diffused and bigger swaths of unsteady fluid, with much higher values of TKE.

At the centre plane (Figure 14) both simulations and PIV measurements predict remarkably similar distribution of TKE. Data captured from the  $Re_p = 500$  experiment indicates the presence of four shear layers on both sides of the jets exiting the bed via the interstices around the sphere in the centre. The areas located on the outside of the jets have significantly weaker TKE content, presumably due to the stabilising influence of the near wall flow. The numerical results show a very similar pattern, however, the value of TKE is underestimated. Although for the lower  $Re_p$  in the PIV data only two regions of high TKE are clearly visible, it can be inferred by comparing to the computed

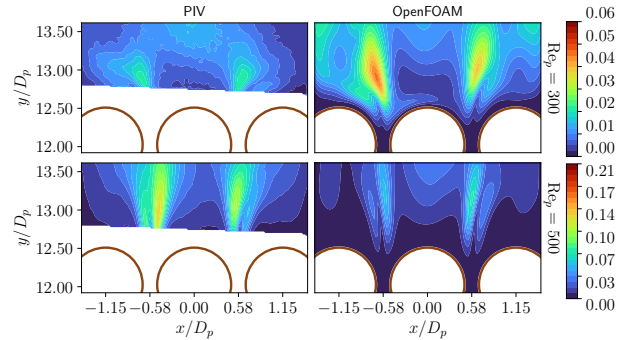


FIG. 14. The normalised TKE  $k/\langle v \rangle^2$ : a comparison between the PIV measurements (left) and the results of the simulation (right) for  $Re_p = 300$  (top row) and 500 (bottom) above the bed surface at the centre plane (see Figure 3). Mind the different colour bars for different  $Re_p$ . The positions of spheres in 21<sup>st</sup> layer is annotated on each graph. In case of PIV measurements, white colour denotes area where the velocity was not captured by the camera.

distribution of TKE that the behaviour of the flow field is analogous to the higher Reynolds number case. The simulation results overpredict the value of  $k$  inside the inner shear layers, however, it also predicts two smaller regions of increased TKE, located around the outer sides of the jets, which get transported towards the walls by the velocity field (see Figure 10). This behaviour is in line with what can be observed in the data available in the PIV measurements.

The same comparison, in a quantitative way, can be made using the data displayed in Figure 15, where the TKE is plotted along the  $y = 12.8D_p$  line in both front and centre planes. As discussed before, for  $Re_p = 300$  the simulated result predict much more diffused distribution of the TKE: the three peaks observed in the PIV data are not present. At the centre plane, the PIV data clearly indicates the presence of the two pairs of the shear layers as pointed out in the previous paragraph. The simulated distribution of TKE is asymmetric with much more pronounced unsteady behaviour near the left jet. However, the  $k$  computed for the right side of the freeboard aligns very well with the measured data, with the peaks of TKE overpredicted by around 50%.

For the higher  $Re_p$ , as mentioned previously, the distribution of TKE is predicted very accurately in the middle of the freeboard on both measurement planes. The high TKE regions visible in the PIV data near the walls, at the front plane, are merged together resulting in a strongly overestimated  $k$ . As a whole, the computed TKE field clearly shares the same features as the measured distribution. Contrary to the results obtained for the lower  $Re_p$  the value of the TKE predicted in the centre plane is mostly underestimated, however, the peaks related to the shear layers are reproduced well in the simulations results.

Overall, the computed distribution of TKE are in a very good agreement with the PIV data, considering the limitation of both the experimental setup and the simulation (discussed below).

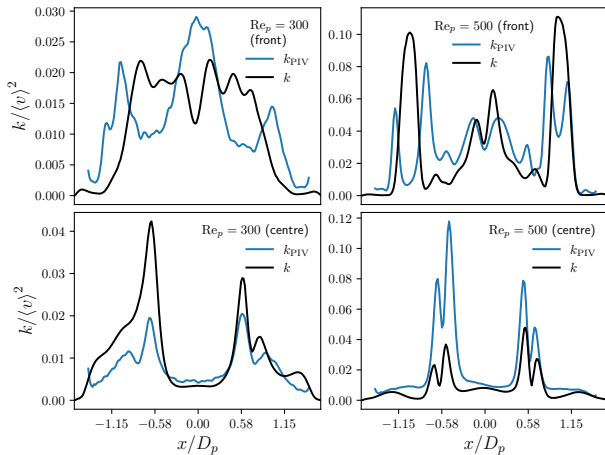


FIG. 15. Comparison of the normalised TKE  $k/\langle v \rangle^2$  for  $Re_p = 300$  and  $500$ , at the front and centre planes, plotted at  $y = 12.8D_p$ .

## E. Discussion

Based on the current simulation results, the wall-channelling effect has a strong influence over the whole flow, dictating the distribution of the velocity both inside and over the bed. Above the bed, the simulated and measured results are in good agreement. The differences can be attributed to several effects:

- i) The modification of the geometry required for the meshing process could increase the velocity of the fluid flowing out of the packing by reducing the interstitial space. With that said, based on the comparisons of the interstitial flow, the chosen geometry simplification method seems to have a low impact on the accuracy of the results, but allow a more robust numerical setup. Since it is observed that the flow near the two topmost layers of spheres can have an influence on the conditions over the bed, there is, however, a chance that the simplification of geometry in this region can result in small discrepancies between the numerics and the simulation.
- ii) The small inaccuracies in the dimensions of the experimental rig, resulting, among others, from the use of an adhesive to stabilise the positions of the spheres, might lead to small differences between the numerical and experimental geometries as visible, for example, in Figure 7. The results measured by PIV have noticeable, but mostly inconsequential, imperfections, e.g. the breaking of symmetry of the measured velocity fields, which might be caused by the geometrical inaccuracies. We assume that such effects, which are also visible in the freeboard, can be perhaps attributed to these small shifts in the placement of the spheres.
- iii) The mesh resolution chosen for the study strikes a balance between the required high accuracy and acceptable computation time to gather a sufficient amount of statistics describing the flow. The narrowest gap between the spheres in the topmost layer is discretised

with around 10 cells (including the boundary layer mesh). It is possible that the resolution in these gaps in the top layers was not sufficient to fully resolve the gradients, leading to increased numerical diffusion and smearing of the ejected jets. A mesh resolution study, perhaps in a simplified setting, would be an important point of investigation for further studies of the described and similar configurations.

- iv) The slight asymmetry of both experimental and simulated results can also be attributed to insufficiently converged mean velocity. The flow above the bed is dominated by low frequency oscillations and flapping motion<sup>21</sup>. The simulations were performed in such a way to enable the biggest possible statistical sample and match the averaging time of the experimental system. However, observing the simulated TKE profile, it can be judged that more averaging time is certainly required for second-order statistics to converge.

The simulated results allow for the inspection of the unsteady behaviour in areas unavailable for the optical measurement techniques, and seem to indicate that the onset of unsteady flow is located slightly below the top surface of the packing. The spots of high TKE remain localised around the jets, potentially due to the constrained geometry of the model packed-bed. A packing with a bigger cross-section area w.r.t. the sphere size should be investigated to determine if, in such a setup, the flow over the bed would become more unstable. The experimental measurements and the computed results for both  $Re_p$  indicate that the flow near the walls remains mostly steady up until  $y = 13.5D_p$ . The only exception to that is the centre plane at  $Re_p = 300$ , where the TKE near the walls is generated by the jets being convected towards the walls. This result seems to indicate that the walls have an overall stabilising effect on the unsteady flow field, which reinforces the necessity for an analysis of a bigger packing.

The fact that the presented numerical setup results in a symmetric flow field in the A1/20 region of interest, along with very well reproduced measurement results in other interstices, indicate that the simulation is able to capture the flow conditions inside the bed with remarkable accuracy, even if the geometry of the packing is simplified. On the other hand, the fact that the results of the simulation are in agreement with the data measured in the packing with geometrical imperfections resulting from the assembly process reinforces that such an experimental approach is a robust and accurate method.

Overall, the flow inside the bed is dominated by the presence of recirculation regions, whose shape and position are mainly influenced by the wall-channeled fluid, which forces the flow into the interstices and in the direction of the centre of the packing. Examining and understanding the behaviour of these separated regions is important from the point of view of potential heat transfer inside the bed, or more generally, mixing of species, as these phenomena can lead to the presence of hotspots and uneven mixing processes. Although, the current work does not attempt to perform such an in-depth analysis of scalar mixing, the presented study of the flow inside the packing shows the possibilities of investigating such flow proper-

ties when a PRS is performed with conjunction with the experimental measurements.

## VI. CONCLUSIONS

In this study, Large Eddy Simulations were performed encompassing a packed bed and its freeboard in the same configuration as investigated experimentally by Velten and Zähringer<sup>1</sup> using PIV, whereby a polyhedral, boundary conforming mesh is employed to discretise the computational domain.

The simulated results compare very favourably with the data captured by PIV, both inside and above the bed, however, small discrepancies between data sets are visible. It can be argued that the reasons for this are twofold. On one hand, an exact reproduction of the experimental geometry was not possible due to the measures taken to stabilise the packing as described in Section II. On the other hand, the presence of low-frequency flow structures developing in the freeboard and also observed in Sadowski *et al.*<sup>15</sup>, Neeraj *et al.*<sup>21</sup> is deemed responsible for a very slow convergence of the statistics.

Nevertheless, based on the gathered data, the particle-resolved simulation conducted with the presented numerical setup has been seen to be a reliable tool for the assessment of the flow conditions inside the packed bed. Combining the CFD-generated prediction with the experimental measurements in the optically accessible interstices allows for the validation of the CFD model and an in-depth analysis of the flow field, as the areas unavailable to PIV can be potentially examined using the validated simulation data. The simplification of the contact regions between the individual spheres by means of the bridging method (described in Section III) allows for very accurate prediction of the interstitial flow while sensibly reducing the problems related to mesh quality.

The flow investigated in the present work is, however, heavily dominated by wall-channelling effects, which steers both the flow inside the bed and in the freeboard, particularly determining the unsteady behaviour over the packing. The jets of faster fluid ejected from the interstices near the walls are the most important features of freeboard flow and generate unsteady recirculation regions in the middle, above the packing. The onset of the transient flow seems to be positioned below the crests of the spheres in the top layer, indicating a complex behaviour of the fluid in the freeboard. To further investigate the flow over the packed-beds, an experimental configuration with a larger size-to-sphere diameter ratio should be investigated both experimentally and numerically, as it would allow for the decrease of the wall influence on the flow conditions.

## ACKNOWLEDGMENTS

The authors gratefully acknowledge the financial support of the Deutsche Forschungsgemeinschaft (DFG) thorough SFB/TRR287, Project Number 422037413 The authors also gratefully acknowledge the Gauss Centre for Supercomputing e.V. (<https://www.gauss-centre.eu>)

for providing computing time on the GCS Supercomputer SuperMUC-NG at the Leibniz Supercomputing Centre (<https://www.lrz.de>).

## DATA AVAILABILITY STATEMENT

The data that support the findings of this study are available from the corresponding author upon reasonable request.

## REFERENCES

- <sup>1</sup>C. Velten and K. Zähringer, "Flow Field Characterisation of Gaseous Flow in a Packed Bed by Particle Image Velocimetry," *Transport in Porous Media* (2023), 10.1007/s11242-023-02010-7.
- <sup>2</sup>A. Shiehnejadhesar, R. Mehrabian, R. Scharler, G. M. Goldin, and I. Obernberger, "Development of a gas phase combustion model suitable for low and high turbulence conditions," *Fuel* **126**, 177–187 (2014).
- <sup>3</sup>A. G. Dixon and B. Partopour, "Computational Fluid Dynamics for Fixed Bed Reactor Design," *Annual Review of Chemical and Biomolecular Engineering* **11**, 109–130 (2020).
- <sup>4</sup>A. G. Dixon, M. Nijemeisland, and E. H. Stitt, "Packed Tubular Reactor Modeling and Catalyst Design using Computational Fluid Dynamics," in *Advances in Chemical Engineering*, Vol. 31 (Elsevier, 2006) pp. 307–389.
- <sup>5</sup>N. Jurtz, M. Kraume, and G. D. Wehinger, "Advances in fixed-bed reactor modeling using particle-resolved computational fluid dynamics (CFD)," *Reviews in Chemical Engineering* **35**, 139–190 (2019).
- <sup>6</sup>A. Shams, F. Roelofs, E. Komen, and E. Baglietto, "Large eddy simulation of a nuclear pebble bed configuration," *Nuclear Engineering and Design* **261**, 10–19 (2013).
- <sup>7</sup>A. Shams, F. Roelofs, E. Komen, and E. Baglietto, "Numerical simulations of a pebble bed configuration using hybrid (RANS-LES) methods," *Nuclear Engineering and Design* **261**, 201–211 (2013).
- <sup>8</sup>A. Shams, F. Roelofs, E. Komen, and E. Baglietto, "Quasi-direct numerical simulation of a pebble bed configuration, Part-II: Temperature field analysis," *Nuclear Engineering and Design* **263**, 490–499 (2013).
- <sup>9</sup>A. Shams, F. Roelofs, E. Komen, and E. Baglietto, "Quasi-direct numerical simulation of a pebble bed configuration. Part I: Flow (velocity) field analysis," *Nuclear Engineering and Design* **263**, 473–489 (2013).
- <sup>10</sup>A. Shams, F. Roelofs, E. Komen, and E. Baglietto, "Improved delayed detached eddy simulation of a randomly stacked nuclear pebble bed," *Computers & Fluids* **122**, 12–25 (2015).
- <sup>11</sup>Y. Jin, M.-F. Uth, A. V. Kuznetsov, and H. Herwig, "Numerical investigation of the possibility of macroscopic turbulence in porous media: a direct numerical simulation study," *Journal of Fluid Mechanics* **766**, 76–103 (2015).
- <sup>12</sup>M.-F. Uth, Y. Jin, A. V. Kuznetsov, and H. Herwig, "A direct numerical simulation study on the possibility of macroscopic turbulence in porous media: Effects of different solid matrix geometries, solid boundaries, and two porosity scales," *Physics of Fluids* **28** (2016), 10.1063/1.4949549.
- <sup>13</sup>F. Rao and Y. Jin, "Possibility for survival of macroscopic turbulence in porous media with high porosity," *Journal of Fluid Mechanics* **937** (2022), 10.1017/jfm.2022.87.
- <sup>14</sup>J. Lage, M. De Lemos, and D. Nield, "Modeling Turbulence in Porous Media," in *Transport Phenomena in Porous Media II* (Elsevier, 2002) pp. 198–230.
- <sup>15</sup>W. Sadowski, M. Sayyari, F. Di Mare, and H. Marschall, "Large eddy simulation of flow in porous media: Analysis of the commutation error of the double-averaged equations," *Physics of Fluids* **35**, 055121 (2023).
- <sup>16</sup>W. P. Breugem and B. J. Boersma, "Direct numerical simulations of turbulent flow over a permeable wall using a direct and a continuum approach," *Physics of Fluids* **17**, 025103 (2005).

- <sup>17</sup>Y. Kuwata and K. Suga, "Lattice Boltzmann direct numerical simulation of interface turbulence over porous and rough walls," *International Journal of Heat and Fluid Flow* **61**, 145–157 (2016).
- <sup>18</sup>A. Shams, F. Roelofs, E. Komen, and E. Baglietto, "Large eddy simulation of a randomly stacked nuclear pebble bed," *Computers & Fluids* **96**, 302–321 (2014).
- <sup>19</sup>S. Rebughini, A. Cuoci, and M. Maestri, "Handling contact points in reactive cfd simulations of heterogeneous catalytic fixed bed reactors," *Chemical Engineering Science* **141**, 240–249 (2016).
- <sup>20</sup>C. Gorges, M. Brömmner, C. Velten, S. Wirtz, E. I. Mahiques, V. Scherer, K. Zähringer, and B. van Wachem, "Comparing two ibm implementations for the simulation of uniform packed beds," *Particology* **86**, 1–12 (2024).
- <sup>21</sup>T. Neeraj, C. Velten, G. Janiga, K. Zähringer, R. Namdar, F. Varnik, D. Thévenin, and S. A. Hosseini, "Modeling Gas Flows in Packed Beds with the Lattice Boltzmann Method: Validation Against Experiments," *Flow, Turbulence and Combustion* **111**, 463–491 (2023).
- <sup>22</sup>J. Wongkham, T. Wen, B. Lu, L. Cui, J. Xu, and X. Liu, "Particle-resolved simulation of randomly packed pebble beds with a novel fluid-solid coupling method," *Fusion Engineering and Design* **161**, 111953 (2020).
- <sup>23</sup>M. Giese, K. Rottschäfer, and D. Vortmeyer, "Measured and modeled superficial flow profiles in packed beds with liquid flow," *AIChE Journal* **44**, 484–490 (1998).
- <sup>24</sup>G. D. Wehinger, *Particle-resolved CFD simulations of catalytic flow reactors*, Doctoral, TU Berlin (2016).
- <sup>25</sup>M. Morales, C. W. Spinn, and J. M. Smith, "Velocities and effective thermal conductivities in packed beds," *Industrial & Engineering Chemistry* **43**, 225–232 (1951).
- <sup>26</sup>C. E. Schwartz and J. M. Smith, "Flow distribution in packed beds," *Industrial & Engineering Chemistry* **45**, 1209–1218 (1953).
- <sup>27</sup>G. Blois, G. H. Sambrook Smith, J. L. Best, R. J. Hardy, and J. R. Lead, "Quantifying the dynamics of flow within a permeable bed using time-resolved endoscopic particle imaging velocimetry (epiv)," *Experiments in Fluids* **53**, 51–76 (2012).
- <sup>28</sup>A. J. Sederman, M. L. Johns, A. S. Bramley, P. Alexander, and L. F. Gladden, "Magnetic resonance imaging of liquid flow and pore structure within packed beds," *Chemical Engineering Science* **52**, 2239–2250 (1997).
- <sup>29</sup>T. Suekane, Y. Yokouchi, and S. Hirai, "Inertial flow structures in a simple-packed bed of spheres," *AIChE Journal* **49**, 10–17 (2003).
- <sup>30</sup>P. Lovreglio, S. Das, K. A. Buist, E. A. J. F. Peters, L. Pel, and J. A. M. Kuipers, "Experimental and numerical investigation of structure and hydrodynamics in packed beds of spherical particles," *AIChE Journal* **64**, 1896–1907 (2018).
- <sup>31</sup>D. Pokrajac and C. Manes, "Velocity measurements of a free-surface turbulent flow penetrating a porous medium composed of uniform-size spheres," *Transport in Porous Media* **78**, 367–383 (2009).
- <sup>32</sup>S. Khayamyan, T. S. Lundström, P. Gren, H. Lycksam, and J. G. I. Hellström, "Transitional and turbulent flow in a bed of spheres as measured with stereoscopic particle image velocimetry," *Transport in Porous Media* **117**, 45–67 (2017).
- <sup>33</sup>S. Khayamyan, T. S. Lundström, J. G. I. Hellström, P. Gren, and H. Lycksam, "Measurements of transitional and turbulent flow in a randomly packed bed of spheres with particle image velocimetry," *Transport in Porous Media* **116**, 413–431 (2017).
- <sup>34</sup>I. A. S. Larsson, T. S. Lundström, and H. Lycksam, "Tomographic piv of flow through ordered thin porous media," *Experiments in Fluids* **59** (2018), 10.1007/s00348-018-2548-6.
- <sup>35</sup>L. F. Gladden, B. S. Akpa, L. D. Anadon, J. J. Heras, D. J. Holland, M. D. Mantle, S. Matthews, C. Mueller, M. C. Sains, and A. J. Sederman, "Dynamic mr imaging of single- and two-phase flows," *Chemical Engineering Research and Design* **84**, 272–281 (2006).
- <sup>36</sup>C. Poelma, "Measurement in opaque flows: a review of measurement techniques for dispersed multiphase flows," *Acta mechanica* **231**, 2089–2111 (2020).
- <sup>37</sup>Y. A. Hassan and E. E. Dominguez-Ontiveros, "Flow visualization in a pebble bed reactor experiment using piv and refractive index matching techniques," *Nuclear Engineering and Design* **238**, 3080–3085 (2008).
- <sup>38</sup>P. Kováts, D. Thévenin, and K. Zähringer, "Experimental investigation of flow fields within cavities of coarse packed bed," *Fachtagung "Lasermethoden in der Strömungsmesstechnik"*, 54–1–7 (8.-10. September 2015).
- <sup>39</sup>F. Martins, C. Da Carvalho Silva, C. Lessig, and K. Zähringer, "Ray-tracing based image correction of optical distortion for piv measurements in packed beds," *Journal of Advanced Optics and Photonics* **1**, 71–94 (2018).
- <sup>40</sup>C. Velten, M. Ebert, C. Lessig, and Katharina Zähringer, "Ray tracing particle image velocimetry – challenges in the application to a packed bed," *Particology* **84**, 194–208 (2024).
- <sup>41</sup>S. Whitaker, *The Method of Volume Averaging*, edited by J. Bear, Theory and Applications of Transport in Porous Media, Vol. 13 (Springer Netherlands, Dordrecht, 1999).
- <sup>42</sup>H. Jasak, *Error Analysis and Estimation for the Finite Volume Method with Applications to Fluid Flows*, Doctoral, Imperial College, London (1996).
- <sup>43</sup>F. Moukalled, L. Mangani, and M. Darwish, *The Finite Volume Method in Computational Fluid Dynamics: An Advanced Introduction with OpenFOAM® and Matlab*, Fluid Mechanics and Its Applications, Vol. 113 (Springer International Publishing, Cham, 2016).
- <sup>44</sup>E. Komen, L. Camilo, A. Shams, B. Geurts, and B. Koren, "A quantification method for numerical dissipation in quasi-DNS and under-resolved DNS, and effects of numerical dissipation in quasi-DNS and under-resolved DNS of turbulent channel flows," *Journal of Computational Physics* **345**, 565–595 (2017).
- <sup>45</sup>ANSYS, Inc., *ANSYS Fluent User's Guide, Release 2023 R2* (2023).
- <sup>46</sup>E. Komen, A. Shams, L. Camilo, and B. Koren, "Quasi-DNS capabilities of OpenFOAM for different mesh types," *Computers & Fluids* **96**, 87–104 (2014).
- <sup>47</sup>R. I. Issa, "Solution of the implicitly discretised fluid flow equations by operator-splitting," *Journal of Computational Physics* **62**, 40–65 (1986).
- <sup>48</sup>LaVision GmbH, "8.4 davis software manual," (Jul-2019).
- <sup>49</sup>D. C. Wilcox, *Turbulence modeling for CFD*, 3rd ed. (DCW Industries, La C nada, Calif, 2006).